High resolution electron microscopy of dislocation ribbons in a CMSX-4 superalloy single crystal

V.A. Vorontsov [d], L. Kovarik [b], M.J. Mills [c], C.M.F. Rae [a]

[a] *Department of Materials Science and Metallurgy, University of Cambridge, Pembroke Street, Cambridge, CB2 3QZ, UK*

[b] *WR Wiley Environmental Molecular Sciences Laboratory, Pacific Northwest National Laboratory, Richland, WA 99352, USA*

[c] *Department of Materials Science and Engineering, The Ohio State University, 2041 College Road, Columbus, OH 43210, USA*

[d] *Department of Materials, Royal School of Mines, Imperial College, Prince Consort Road, South Kensington, London SW7 2BP, UK*

Abstract

High-resolution scanning transmission electron microscopy (HR STEM) has been used to study the structure of dislocations in single crystal superalloy samples that have been subjected to conditions that favour the primary creep regime. The study has revealed the detailed structure of extended $\frac{a}{2}\langle 112\rangle$ dislocations as they shear the γ' precipitates during creep. These dislocations dissociate in a manner that is consistent with predictions made using the Phase Field Model of Dislocations (PFMD) and also suggests the importance of the reordering process during their movement. The shearing done by the $a\langle 112\rangle$ dislocations was also found to distort the γ/γ' interface, changing its appearance from linear to a 'saw tooth' pattern. Another important observation was the segregation of alloying element with high atomic mass to the stacking faults, presumably to reduce their energies during shear. Numerous $\frac{a}{2}\langle 110\rangle$ dissociated dislocations were also observed in the γ channels of the superalloy. The high resolution provided by the STEM imaging enables one to study the high energy faults that are usually difficult to observe in conventional weak-beam TEM, such as CISF and CESF-1 in the γ' and the ISF in the γ, and to make estimates of their energies.

Key words: STEM; Primary creep; Dislocation dissociation; Shockley partials; Stacking faults;

1 Introduction

Nickel-base superalloy single crystals exhibit superior creep resistance at elevated temperatures, which makes them the most suitable materials for the manufacture of turbine blades in aero engines. They employ a number of strengthening mechanisms [1], (*i.e.* order, misfit, precipitation, solute and stacking fault strengthening), to significantly inhibit dislocation glide, which gives rise to the superb mechanical properties over a wide range of temperatures. To facilitate cost-effectiveness and timely alloy design, it is crucial to develop an understanding of the complex dislocation interactions that take place within the microstructure of a superalloy. More importantly, a good understanding of alloying effects on these interactions is essential for achieving the desired price/performance ratio for any new alloy.

In this work, we consider in detail the structure of dislocations when a superalloy single crystal is deformed under conditions favouring primary creep at intermediate temperatures (in the range 750°C) [2] and the effect of these dislocations on the microstructure. The main source of creep strain in this regime is the propagation of $a\langle 112\rangle$ dislocation ribbons through both γ and γ' phases [3]. The structure of these dislocations and their role in viscous slip of superalloys was originally discussed by Kear *et al.* [4,5]. TEM studies [3,6] have shown that the $\frac{a}{2}\langle 112\rangle$ dislocations making up the $a\langle 112\rangle$ ribbon are dissociated into partial dislocations enclosing a low energy superlattice intrinsic or extrinsic stacking fault (SISF and SESF respectively). According to these studies, the dissociation of a complete $a\langle 112\rangle$ ribbon in the γ' would take place according to the following scheme:

$$2\times\frac{a}{2}[\bar{1}12]\rightarrow\frac{a}{3}[\bar{1}12]+\mathbf{SISF}+\frac{a}{6}[\bar{1}12]+\mathbf{APB}+\frac{a}{6}[\bar{1}12]+\mathbf{SESF}+\frac{a}{3}[\bar{1}12] \quad (1)$$

It should be noted, that the $a\langle 112\rangle$ dislocation is rarely observed passing through a single γ' precipitate in its entirety. Instead, to avoid the high APB energy, the constituent $\frac{a}{2}\langle 112\rangle$ dislocations occupy adjacent precipitates where they are separated by perfect crystal in the γ matrix. In addition, the theoretical discussion of Kear *et al.* in references [4,5], proposes that the $\frac{a}{3}\langle 112\rangle$ superpartials may each be dissociated into two $\frac{a}{6}\langle 112\rangle$ Shockley partials separated by either intrinsic or extrinsic complex stacking faults. Thus, the complete dissociation sequence is as follows:

$$\begin{aligned}2\times\frac{a}{2}[\bar{1}12]\rightarrow&\frac{a}{6}[\bar{1}12]+\mathbf{CESF-1}+\frac{a}{6}[\bar{1}12]+\mathbf{SISF}+\frac{a}{6}[\bar{1}12]+\\&\mathbf{APB}+\frac{a}{6}[\bar{1}12]+\mathbf{SESF}+\frac{a}{6}[\bar{1}12]+\mathbf{CISF}+\frac{a}{6}[\bar{1}12]\end{aligned} \quad (2)$$

where CISF is a complex intrinsic stacking fault and CESF-1 is a complex

extrinsic stacking fault with high-energy bonding violation on one side of the fault. The structure of the latter can be thought of as SISF over CISF. Both atomistic simulations [7] and the Phase Field Model of Dislocations (PFMD) [8–10] have shown that the $\frac{a}{3}\langle 112\rangle$ dislocations are indeed likely to be dissociated. Both complex faults have a very high fault energy [11], and as a result the bounding Shockley partial pair would have such a small separation that when observed using conventional TEM imaging, they would appear as a single $\frac{a}{3}\langle 112\rangle$ dislocation. Link and Feller-Kniepmeier [12] remarked on this difficulty in distinguishing these Shockley partials. However, a subsequent TEM study by Link [13] showed the ribbon-like appearance of $\frac{a}{3}\langle 112\rangle$ dislocations in SRR-99 single crystals, which suggested that these superpartials are indeed dissociated. Since these high-energy complex faults would be formed at both leading and trailing edges of the dissociated $a\langle 110\rangle$ and $a\langle 112\rangle$ superdislocations, they may have a significant effect on the mobility of these dislocations. It has also recently been proposed by Kovarik *et al.* [14–16] that the movement of dislocation configurations involving net $\frac{a}{3}\langle 112\rangle$ displacements through the γ' phase may be controlled by local, diffusion-mediated reordering of the high energy faults, converting them into lower energy configurations. Thus, direct observation of the partial dislocation configurations at the atomic scale are sought to improve the understanding of the rate-controlling processes in these important alloys.

At larger magnifications and using favourable viewing directions, evidence of the presence of complex faults at the outer edges of $\frac{a}{2}\langle 112\rangle$ dislocation ribbons can indeed be observed. This was found in a preliminary study shown in Figure 1. A constricted (presumably complex) stacking fault can be seen preceding an extended stacking fault. These small faults were observed in two commercial superalloys (TMS-82+ and TMS-75), that have undergone primary creep at 750 °C and 750 MPa. To confirm that these are truly individual stacking faults atomic resolution imaging is required. Recent technological advances have made the necessary sub-nanometre HR STEM an accessible technique for imaging the atomic columns.

Aberrations associated with electromagnetic lenses become more profound as the image magnification is increased [17]. This limits the resolution of conventional TEM. In particular, chromatic aberration becomes a problem as the specimen thickness increases. In STEM, the resolution is limited by the quality and size of the focused electron probe, while magnification is controlled simply by varying the area of the sample scanned by that probe. Thus, the ability to obtain a fine and coherent probe is paramount in HR STEM. Recent improvements in spherical aberration correction of the probe-forming lens, as used on the FEI Titan^3 in this work, enables atomic scale imaging in close packed metals along close packed zones.

STEM also offers atomic mass contrast (Z-contrast) capability, which is achieved

through the use of a high-angle annular dark-field (HAADF) detector. This type of detector collects electrons scattered by the sample foil at high angles, greater than 50 milliradians. At such great angles, the interference from Bragg scattering becomes negligible, and most of the signal intensity arises from elastic Rutherford scattering that is sensitive only to the atomic mass. Given a sufficiently small electron probe and correct specimen-beam alignment, this isolation of Z-contrast enables atomic resolution. The inter-atomic spaces are regions of very low Z and thus appear darker in the image. In HAADF images the contrast is relatively unaffected by small changes in objective lens defocus and specimen thickness. This gives Z-contrast imaging an advantage over phase-contrast imaging when it comes to atomic-resolution characterisation, as the former are simpler to interpret reliably.

This paper is structured with the presentation of several important dislocation structures in a crept test-piece of the alloy CMSX-4, an important commercial single crystal superalloy. There follows a discussion of the implications of these observations on the formation and movement of dislocations causing stacking fault shear.

2 Experimental method

2.1 Sample crystal orientation and creep deformation

A test specimen was machined from the commercial single crystal superalloy CMSX-4. Its tensile axis deviated from the [001] direction by 12.7 ° along an axis 24.4 ° from the (100) plane. This misalignment is illustrated by the stereogram shown in Figure 3. The sample was subjected to tensile creep at a temperature of 750 °C and stress of 750 MPa, (*i.e.* conditions favouring the primary creep regime). The primary slip system having maximal Schmid factor under this tensile axis is the $[1\bar{1}2](\bar{1}11)$ slip system. The test was interrupted after 8.6% creep strain had been accumulated over 8 hours. At the point of interruption, the material had completed primary creep and had been undergoing secondary creep for approximately two hours. The corresponding creep curve illustrating this is shown Figure 2.

Laue X-ray imaging was employed to determine the primary slip plane of the crept test specimen. This allowed the sectioning of the crystal in two different ways in order to fully characterise the dislocation structures, as shown in Figure 3. The first view (indicated as "TEM image" in Figure 3) was created by sectioning parallel to $(\bar{1}10)$, enabling the dislocation structures on the primary $[1\bar{1}2](\bar{1}11)$ slip system to be observed at approximately 37° to the foil normal. This view allowed for convenient characterisation of overall dislocation Burgers

vectors and line directions using conventional, diffraction contrast techniques. The second sectioning plane (STEM HAADF0 Section) was parallel to the tensile axis while having the primary $(\bar{1}11)$ slip plane oriented perpendicular to the foil normal and the primary $[1\bar{1}2]$ Burgers vector lying in the plane of the foil. This way, any pure edge dislocation in this slip system would have its line direction parallel to the foil normal, [110].

The described sectioning procedure for single crystal was chosen with the intention of imaging the core structure of the partial edge dislocations passing within the slip plane perpendicular to foil. This would allow the imaging of [110] atomic columns and make for convenient identification of the stacking faults. In turn, the dislocations would be identifiable from the stacking fault terminations. The specimen viewing direction relative to the primary slip plane and slip system with the largest Schmid factor is shown in Figure 4. Thin foil specimens were prepared by spark erosion and subsequent electropolishing with a 6% perchloric acid solution in methanol (10% solution using 60% perchloric acid stock) at 18 V and -10 °C.

Conventional TEM imaging was performed on specimens cut along the long axis of the test-piece perpendicularly to the STEM image plane (see Figure 3). Figure 5 shows the microstructure of the alloy populated with numerous dislocations and stacking faults in both the matrix and precipitate phases. The majority of the stacking faults in the γ' lie on the major slip plane. However, it was found that the Burgers vectors terminating these faults were not exclusively of the slip system with the highest Schmid factor, $[1\bar{1}2](\bar{1}11)$. APB pairs exhibiting a wavy morphology can also be seen.

2.2 Imaging and analysis

HR STEM was performed on a thinned section of the crept CMSX-4 single crystal prepared as described in the previous section. An FEI Titan^3 STEM featuring a monochromator and a probe aberration corrector was used to perform the HAADF imaging.

Although the HAADF imaging itself is capable of resolving the atomic columns in the thinner regions of the sample, the obtained digital images were subjected to a number of processing steps and numerical analysis in order to enhance and emphasise the observed features. The purpose of the analysis was to locate and identify the degree of centro-symmetry for each atomic column and thus identify faults in the stacking sequence.

All the stages of the processing sequence were performed using MATLAB® with the Imaging Processing Toolbox. The processing sequence is as follows:

(1) Filter noisy image using a "top hat" filter.
(2) Perform a de-convolution of the image with a Gaussian kernel of size σ_1, to enhance the signal to noise ratio in the underlying lattice.
(3) Re-convolute the image with a Gaussian kernel of size $\sigma_2 < \sigma_1$.
(4) Identify and tabulate the 2D coordinates of the atomic columns for centre of symmetry analysis.

Once the tabulated spatial coordinates of the atomic columns were obtained, a centre of symmetry analysis was performed. When reading in the x, y position of each atomic column, we can assign it a unique sequential number n. In a perfect crystal, each atomic column (and hence each point, n) will be surrounded by six nearest neighbour columns. The centre of symmetry analysis used in this study is based on the procedure outlined by Li [18]. It is carried out using the following sequence of steps:

(1) Calculate the distances between each atomic column and all other neighbours.
(2) Identify the six nearest neighbours.
(3) Rank the neighbours 1 to 6 in order of increasing distance. Let the rank be denoted by r.
(4) Taking the central point, n, as the origin, calculate the relative position vector, $\mathbf{d}_r$, of each neighbour.
(5) Take the first neighbour, $\mathbf{d}_1$, and search among the remaining five neighbours to find the smallest $D = |\mathbf{d}_1 - \mathbf{d}_j|^2$. Call this minimum D_1. Given the non regular hexagonal arrangement of the nearest neighbours in a perfect crystal, the $\mathbf{d}_j$ that gives the smallest D will be on the opposite corner of the hexagon to $\mathbf{d}_1$. In a perfect crystal, D will be zero, since $\mathbf{d}_j$ will lie on the straight line running through $\mathbf{d}_1$ and the origin at point n.
(6) Repeat the previous step with each of the remaining five neighbours to obtain the full set of minimum vector sums, D_1 to D_6.
(7) Calculate the centre of symmetry parameter, M_n, as given by the following equation:

$$M_n = \frac{1/2 \times \sum_{r=1}^{6} D_r}{2 \times \sum_{r=1}^{6} |\mathbf{d}_r|^2} \tag{3}$$

It can be seen from the equation that the crystal deviates from centro-symmetry when a stacking fault is present and the original (non regular) hexagonal arrangement is lost. This gives non-zero values of M_n for the atomic columns in the fault.

The points on the edges of the images do not have six neighbours. Therefore, an exclusion zone must be specified around the edge so that only points with six neighbours are considered in the centre of symmetry analysis. In addition,

to obtain a 2D density plot of M_n, the points were meshed and the data within each mesh element was interpolated using MATLAB®'s cubic algorithm.

3 Results

This section will discuss the HAADF images of stacking faults lying on the primary slip plane of the single crystal that has been subjected to conditions favouring the primary creep mode. The images were acquired from an electropolished thin foil which was cut to make the image plane coincide with (110) and lie perpendicular to the primary slip plane, $(\bar{1}11)$. Other planes of interest, the $(1\bar{1}1)$ and the (001), also pass vertically through the foil.

The HAADF imaging revealed numerous stacking faults in both the γ and γ' phases. Both intrinsic and extrinsic stacking faults were imaged. The centre of symmetry analysis allows the two to be distinguished with greater clarity than in the raw images. Intrinsic faults appear as two immediately adjacent layers with low centro-symmetry, (high M_n). Extrinsic faults appear as two high M_n layers separated by a single layer with higher centro-symmetry.

3.1 $\frac{a}{2}\langle 110\rangle$ *dislocations at* γ/γ' *interfaces*

Stacking faults observed in the γ channels were largely associated with $\frac{a}{2}\langle 110\rangle$ dislocations. Many could be located at the γ/γ' interface. Examples of a 'horizontal' (001) channel region including several $\frac{a}{2}\langle 110\rangle$ dislocations are shown in the [110] zone axis HAADF images obtained at two different magnifications seen in Figures 6(a) and 6(b). A noteworthy observation apparent at this scale is the effect of the dislocations on the γ/γ' interface. The local stress field of the gliding dislocations has apparently led to a distortion in the plane of the interface, giving it a serrated appearance and causing the interface to locally deviate from the overall (001) for the γ' precipitates. The γ/γ' interface can be identified effectively due to the net atomic number difference between the two phases. The γ phase appears brighter than the γ' phase in overall intensity level, which is expected based on the known solute partitioning to the γ and γ' phases. Indeed, based on atom probe tomography (APT) and EDX microanalysis [19,20], the γ phase in CMSX-4 is richer in the larger atomic number elements Re and W, while the γ' phase is richer with the lighter Al atoms.

In most models for the mechanical properties of superalloys the interface is considered to be flat. However, the present research shows quite clearly that this is not the case, even though the creep temperatures are significantly below

those for which 'rafting' occurs, which is the well-known directional coarsening of the overall precipitate morphology. The effect dislocations have on the boundary plane has been well documented at higher temperatures. Link *et al.*, working at 1100 °C [21], concluded that the deep grooves were formed by the growth of the γ' phase during cooling, but that this mechanism did not operate below 950 °C, because the change in volume fraction was too small. This is not the case here, as there us no net migration of the interface. If a line is drawn through the centres of the dissociated dislocations, it will lie close to the average position of the γ/γ' interface, and roughly equal amounts of each phase would lie on the wrong side of this line. It appears that the serration of the interface arises from local diffusion of the different species to reduce the elastic strain associated with the dislocation. There also appears to be enhanced intensity associated with the location of each dislocation at the interfaces. Based on analysis of the Burgers vector direction described below, the enhanced intensity appears to lie above the plane of dissociation as viewed in this image which is in the tensile region of the dislocation stress field.

The more complex, local interfacial geometry is likely to reduce the climb rate of dislocations around the precipitates at these more modest temperatures as they would need to move with the serrations. The following important observation demonstrates that this is the case. Dislocations lying on either side of the γ channel have opposing 'signs', which is expected since the applied stress should drive dislocations of opposing Burgers vectors to either interface. The dislocation dipoles should be deposited on the interfaces through the glide of an $\frac{a}{2}\langle 110\rangle$ dislocation on the $(\bar{1}11)$ plane. However, it can be readily observed in, for instance, Figure 6(b) that the dislocations are no longer disposed relative to each other on a common $(\bar{1}11)$ plane, proving that they have indeed climbed off of their common glide planes. This climb process presumably occurs as an inherent part of creating the local curvatures at the γ/γ' interfaces.

Figure 7 shows an example of such a complete γ lattice dislocation dissociated at the matrix/precipitate interface. The Burgers circuit drawn around this defect requires a vector of $\frac{a}{4}[1\bar{1}2]$ to be closed in the plane observed,(Figure 7a). This is consistent with a Burgers vector of either $\frac{a}{2}[0\bar{1}1]$ or $\frac{a}{2}[101]$. Both of these Burgers vectors are possible and of the most highly stressed slip systems of the type $\frac{a}{2}\langle 110\rangle(\bar{1}11)$. The partial dislocation on the left of the stacking fault requires a longer vector to close the Burgers circuit, and so it corresponds to $\frac{a}{6}[1\bar{1}2]$ and is therefore an edge dislocation, while the right-hand termination is the 30° $\frac{a}{6}[\bar{1}\bar{2}1]$ partial. This indicates that the lattice dislocation is $\frac{a}{2}[0\bar{1}1]$. The distance separating the two Shockley partials is approximately 18 apparent lattice spacings based on the centre of symmetry plot in Figure 7(b). Their average length is equivalent to that of an $\frac{a}{4}[1\bar{1}2]$ displacement. Thus, using an estimate of the lattice parameter at 750 °C, a_γ=0.3634 nm [22,23], one can estimate the size of the fault, d_{ISF}.

$$d_{\mathrm{ISF}} = 18 \times \sqrt{\frac{3}{8}} \times a_\gamma = 4.006\,\mathrm{nm} \tag{4}$$

The energy of a planar fault, γ, can be related to the spacing between the dislocations enclosing it, d, by the following equation [24]:

$$\gamma = \frac{G}{2\pi d}\left((\mathbf{b}_1 \cdot \xi_1)\,(\mathbf{b}_2 \cdot \xi_2)\,\frac{(\mathbf{b}_1 \times \xi_1) \cdot (\mathbf{b}_2 \times \xi_2)}{1-\nu}\right) \tag{5}$$

where K is a coefficient dependent on the character of the dislocations, G is the shear modulus, $\mathbf{b}$ is the Burgers vector of the dislocations enclosing the fault and ξ is their character vector. Substituting G=105 GPa and ν=0.41 [25], with the vectors $\mathbf{b}_1=\frac{a}{6}[1\bar{1}2]$, $\mathbf{b}_2=\frac{a}{6}[\bar{1}\bar{2}1]$, $\xi_1=[110]$ and $\xi_2=[0\bar{1}1]$ into the above equation , we obtain an estimate of the ISF fault energy of 156 mJ m^{-2}.

This estimate is within the 105-204 mJ m^{-2} range of values predicted using a variety of atomistic calculations for pure nickel [26]. Segregation of high Z elements to the stacking fault is indeed evident in this case. Furthermore, stacking fault energies are lower at elevated temperatures. The alloy was tested at 1023 K whereas the atomistic models assumed a temperature of 0 K. Finally, since the γ/γ' interface is indeed locally rotated parallel to the stacking fault of the dislocation, the actual dissociation distance is expected to be a result of the interaction of several complicating factors, including the γ-γ' misfit and the change in composition across the interface. The heavier (and larger) atoms are clearly concentrated on the upper (brighter) side of the fault in the γ phase in tension. The extra half plane lies in the γ' on the lower side of the fault as viewed in Figure 7(a) to some extent relieving the misfit from the smaller γ' lattice parameter.

3.2 Superlattice faults and terminating partials

Superlattice stacking faults in the γ' were relatively convenient to locate and image in HAADF mode, because of their relatively large size and significant Z-contrast. The enhanced intensity of the atomic columns in the faults indicates extensive segregation of heavier alloying atoms to these defects, which is liable to lower their energy.

In SISFs, the high Z atoms appear to have no preference for any particular sites, see Figure 8. This makes the faults appear relatively uniform and diffuse in brightness. It was also found that, in the wakes of these stacking faults, trails of the heavy elements remain. This is a clear indication that the observed segregation is a diffusional process that requires time and elevated

temperatures to occur. The described phenomenon is likely to be important in determining the rates and threshold stresses for the viscous slip processes taking place during creep.

The SESFs observed in the specimen also showed segregation of heavier alloying elements. However, unlike in the SISFs, this segregation showed less pronounced contrast but was more precise and exhibited significant local order. The high Z elements were found concentrated at specific sites, forming a grid-like pattern. An example of this phenomenon is illustrated in Figure 9. This local ordering is an indication of localised atomic shuffles taking place to create the SESFs in the alloy [14–16].

The majority of the stacking faults observed within the precipitates, were widely extended and could not fit within a single atomic-scale HAADF image. However, the features of greatest interest for this study were the structures at the terminations of the faults at their leading and trailing edges. Most of the faults found in the γ' phase had one of their ends terminating at the γ/γ' interface, although several faults terminating within the γ' were also observed. The structure of the faults and the sample crystallography/orientation indicated these interfacial terminations to be at the trailing edges of the both faults. As shown in Figure 8, the γ/γ' interface plane locally rotates dramatically when a terminating superpartial is located at the interface - a feature that is similar to the serrations on the interfaces caused by the $\frac{a}{2}\langle 110\rangle$ matrix dislocations discussed above. The structures of the SISF and SESF terminations are discussed in greater detail within the following sections.

3.3 Structure of the SISFs terminating in the γ'

Figure 10 shows an example of an SISF termination inside the γ', which is identified as a leading superpartial based on the sample crystallography and orientation. Quite remarkably, this extended intrinsic fault terminates as a narrow extrinsic stacking fault. The local displacements associated with this fault are consistent with the CESF-1 structure predicted by the EAM [11] and PFMD models [9,10]. The Burgers circuit traced around the entire CESF-1 segment requires a closure displacement that is consistent with an edge dislocation on the primary slip system, with $\mathbf{b}=\frac{a}{3}[1\bar{1}2]$. This is $4/3$ of the apparent lattice spacing along the fault, which would give $\mathbf{b}=\frac{a}{3}[1\bar{1}2]$. Completing the Burgers circuit within the extrinsic fault gives an apparent closure failure of approximately half this distance, as expected. The width of the fault can be estimated to be 12 apparent lattice spacings. Taking $a_{\gamma'}= 0.3627\,\text{nm}$ [22,23], we may estimate the width of the fault to be $2.665\,\text{nm}$ at $750\,^{\circ}\text{C}$. Since the stacking fault is bounded by partial dislocations with the same Burgers vector,

we may use the following equation to estimate its energy.

$$\gamma = K\frac{Gb^2}{2\pi d} \tag{6}$$

Using the above equation with G=105 GPa [25] and K=1 we can estimate the CESF-1 energy, $\gamma_{\text{CESF-1}}$=137 mJ m^{-2}, which is lower than the only available reference value of 271 mJ m^{-2} predicted by EAM [11] using the Mishin potential [27].

This observed configuration shows that the $\frac{a}{3}[1\bar{1}2]$ superpartial dissociates into two identical Shockley partials separated by a complex extrinsic stacking fault. This termination structure has important implications in terms of its mobility during high temperature deformation, as is discussed in Section 4. The alternative dissociation scheme, which does not require a fault on two planes, would be to split into three partials $\frac{a}{6}[\bar{1}\bar{2}1]+\frac{a}{6}[1\bar{1}2]+\frac{a}{6}[211]$ separated by a CISF and an APB [4,5]. The findings of this study show that this is not the case during creep.

3.4 Structure of the SISFs terminating in the γ'

Figure 11 shows an extended SESF terminating within a γ' precipitate. It appears to end with a very narrow intrinsic fault, although it is not very distinct from the centre of symmetry analysis. Tracing a Burgers circuit around the end of the SESF requires a closing displacement half that obtained for the SISFs described previously, *i.e.* $\frac{a}{6}[1\bar{1}2]$. There are three possible explanations for this observation:

(1) The extrinsic fault is a CESF-1.
(2) The fault is an SESF but terminates in a $\frac{a}{6}[1\bar{1}2]$ partial leaving an APB in the lattice.
(3) The Burgers vector of the dislocations producing the SESF are angled to the [110] direction. Thus, the possible Burgers vectors would be $\frac{a}{3}[211]$ or $\frac{a}{3}[\bar{1}\bar{2}1]$. (See Figure 4.)

The length of the fault and the high energy of the complex fault rule out the first possibility. Although the APB would not be visible itself, there is no circumstantial evidence for its presence: no additional dislocations close to the end of this fault to terminate the APB. This suggests that the second possibility is unlikely too due to the high energy of the APB. Therefore, the third possibility is the most probable. If the dislocation Burgers vector were to be at 60° to the primary slip system Burgers vector, it would give half the closing displacement expected from the primary system. The source of

this configuration may be the dissociation of a pair of dislocations into the $\frac{a}{3}[211]+\frac{a}{3}[1\bar{1}2]$ superpartial pair, with the former leading the fault. TEM has confirmed that faults associated with these Burgers vectors are present in the sample. For the given specimen, only dislocations trailing the SESF would be of edge character. Dislocations leading a SESF would be of mixed character.

It is evident that the last 7 apparent lattice spacings of the fault have a different structure. The ending of the dislocation is clearly a complex intrinsic fault as revealed by the Burgers circuit drawn around the last few atom columns of the fault but the symmetry analysis highlights only a single layer of atoms showing clear asymmetry rather that the two adjacent layers that a rigid displacement model would predict. Instead the middle layer of the three has adjusted slightly to concentrate the asymmetry onto the lower layer. Taking into account that the dislocations binding this CISF are at 60° to the primary slip system and hence the image plane, the energy of the fault is estimated to be $118\,\mathrm{mJ\,m^{-2}}$. This is a reasonable value as it is smaller than the CESF-1 energy. However, it is substantially lower than the $217\,\mathrm{mJ\,m^{-2}}$ value calculated using EAM in [11] and other experimentally obtained values in single-phase Ni3Al intermetallic compounds which range from 177 to $235\,\mathrm{mJ\,m^{-2}}$ [28,29].

Figure 12(a) shows the general view of another example of a SESF crossing the γ/γ' interface. The extrinsic stacking fault may first be located as a thin horizontal band that is brighter than the surrounding (dark) γ' phase on the right-hand side of the image. There is a visible 'notch' in the γ/γ' interface where it is crossed by the fault. Upon close inspection, it is evident that the fault extends more than halfway into the γ channel. Figure 12(b) shows, the same fault at a higher level of magnification. It should be noted, there is no change in Burgers vector as it crosses the matrix-precipitate interface. This implies that the fault spans both phases continuously, with an SESF structure in the γ' and ESF structure in the γ. Note again the nearly periodic enhanced intensity exhibited in the centre of the SESF.

Figure 13 shows two stacking faults terminating at the γ/γ' interface. The lower of these is intrinsic and lies in the γ phase, while the other is extrinsic and is in the γ' precipitate on the right. The Burgers circuit closure displacement for the end of the SESF is $\frac{a}{6}[1\bar{1}2]$. This is consistent with a partial dislocation of edge character with the said Burgers vector composed of two zonal Shockley partials on adjacent planes since the SESF is spread over two planes. Note that the termination is very abrupt, indicating no separation between the Shockley partials of the zonal configuration. If it were to move to the right and enter the γ' precipitate, an APB fault would be created to the left side of the zonal partial. Alternatively, it may be a 60° mixed dislocation, as has already been discussed. However, as the fault terminates at the γ/γ' interface the first possibility is more probable. In the case of the intrinsic fault which lies in the γ, the closure displacement at the phase boundary is also $\frac{a}{6}[1\bar{1}2]$.

This is consistent with a lattice dislocation which has dissociated into two Shockley partials in the γ as follows:

$$\frac{a}{2}[0\bar{1}1] \rightarrow \frac{a}{6}[1\bar{1}2] + \frac{a}{6}[\bar{1}\bar{2}1] \tag{7}$$

4 Discussion

The STEM imaging discussed in this work has yielded a number of noteworthy observations. First and foremost, the study has provided an insight into the structure of the $\frac{a}{3}\langle 112\rangle$ superpartials at the terminations of $\frac{a}{2}\langle 112\rangle$ dislocations that are the main source of strain accumulation in superalloys subjected to conditions favouring primary creep mode.

The structure of the $\frac{a}{3}\langle 112\rangle$ superpartial terminating the SISF observed in Figure 10 is remarkable since the intrinsic fault is actually terminated by an extrinsic stacking fault. At first, it may not be obvious that this should be the case since it is possible to create a SISF by a fully planar dislocation configuration of three Shockley partials as shown in Figure 14(a). However, the disadvantage of this configuration is that it requires the creation of two high-energy planar defects, the CISF and the APB, while requiring an additional Shockley partial dislocation which bears an associated elastic energy penalty. From this linear configuration the leading extrinsic fault may be created via the transformation of the "Giamei lock" [30], as is shown in Figure 14. In this scenario, the two leading Shockley partials in Figure 14(a) must first cross-slip onto an adjacent glide plane, as shown in Figure 14(b). Following this, the δA and $B\delta$ Shockley partials must exchange relative positions as is illustrated in Figure 14(c). This exchange would create the following configuration: (a) a $\frac{a}{6}\langle 112\rangle$ zonal partial (δC+δA, which is equivalent to $B\delta$ spread on two adjacent (111) planes), followed by (b) a δB partial on a single (111) plane, and finally (c) a two layer fault consisting of an APB over an SISF.

Alternatively the linear configuration may not be the starting point for the formation of the intrinsic stacking faults. This fault is the lead part of the a $a\langle 112\rangle$ ribbon and forms by the combination of two $\frac{a}{2}\langle 110\rangle$ dislocations in the γ channels with Burgers vectors at 60°, based on previous conventional TEM analysis [3]. As illustrated in Figure 15, this would have to occur by the climb of these dislocations in the interface unless, by chance, they were on precisely the same slip plane. The observations of the non-alignment of the dislocation dipoles across the γ channels (*e.g.* Figure 6) shows that climb was active during creep. If the two dislocations approach by climb along the γ/γ' interface the SISF could form as they reach adjacent planes. Figure 15 shows the sequence of events from (a) the two dislocations reaching adjacent planes; (b) the leading partials of the two γ lattice dislocations enter to form a CESF

followed by one of the trailing partials; (c) the fourth partial remains at the interface whilst the reordering process gives a SISF in the γ'.

In either case, the described processes would only be energetically advantageous if the two-layer APB/SISF could be rapidly transformed to a single-layer SISF as the a $\frac{a}{3}\langle 112\rangle$ superpartial propagates through the crystal. Kear *et al.* [4,5] suggested that the necessary elimination of the high-energy nearest neighbour bonds within the two-layer fault must be brought about by an effective dipole displacement near the core of the superpartial. This effective displacement may be attained either via cooperative shear or by means of a diffusive vacancy-mediated atomic shuffling. Kovarik *et al.* [14,16] have put forward a mechanistic theory for the latter based on *ab initio* simulations. According to the scheme proposed by the aforementioned authors, reordering is only possible in the wake of multi-plane configurations with a net Burgers vector of $\frac{a}{3}\langle 112\rangle$. Therefore, the leading extrinsic fault configuration cannot reorder itself to a lower energy configuration and is therefore expected to remain narrowly spread. However, the relatively low energy SISF that follows it can extend across entire γ' precipitates. Since the reordering process is diffusion-controlled, it is expected to be possible only during deformation at higher temperatures. Thus, this scenario provides a natural explanation for the slip mechanisms featuring the viscous motion of $\frac{a}{3}\langle 112\rangle$ superpartials (that can be part of either a $a\langle 112\rangle$ and $a\langle 110\rangle$ dislocations) which is observed at elevated temperatures. Unlike the Gaimei lock which relies on cross-slip, and is only viable for screw orientations, reordering explains the lack of any obvious line direction preference for the $\frac{a}{3}\langle 112\rangle$ dislocations: when controlled by disordering, the mobility of all line directions is expected to be similar to the first order.

The EAM simulations of Yamaguchi *et al.* [7] have simulated an $\frac{a}{3}\langle 112\rangle$ superdislocation core which is spread over multiple glide-planes. The authors found that inter-atomic potentials which produce a very high APB energy stabilise the dissociation of $a\langle 110\rangle$ dislocations into $\frac{a}{3}\langle 112\rangle$ superpartials. The superpartial core configuration depends on the exact assumptions of the calculation but in all cases the core is spread spatially over multiple planes of the crystal. In two configurations, the largest atomic displacements are confined to parallel $\{111\}$ planes. One of these (D2) shows a striking resemblance to the structure observed in Figure 10 with two clearly identifiable Shockley partials bounding it. Using the same inter-atomic potentials, Paidar *et al.* [31] investigated the effect of an applied shear stress on the core structure of the $\frac{a}{3}\langle 112\rangle$ superpartials. All the cores transformed to a double planar configuration but proved sessile, since an atomic shuffle (or re-ordering) is required to eliminate the APB formed in its wake. A more recent EAM study by Voskoboinikov and Rae [32] using the Mishin potential [27] has also found that upon the dissociation of edge superdislocations the SISF and the leading CESF-1 form instantaneously during relaxation.

The structures predicted in the classic works of Yamaguchi *et al.* and Paidar *et al.* remind us that we should not treat dislocations and stacking faults as rigid geometric entities described by discrete displacements. In particular dislocation cores are able to spread over multiple planes, and to be adaptable "fluid" structures that are able to restructure in response to an applied shear stress. This propensity will only be enhanced by increased rates of diffusion at elevated temperatures. An example of this is the structure of the CISF at the termination of the SESF in Figure 11 which did not form a clear intrinsic fault. Furthermore, these studies have shown that core structures are strongly dependent on the inter-atomic forces (potentials), and therefore provide an explanation for the composition dependence of dislocation mechanisms and the mechanical properties that result.

The segregation of heavier alloying elements to the stacking faults is another remarkable observation of the present study. In the case of the SESF, the segregant atoms show a distinct preference for certain sublattice sites within the stacking fault. The resulting grid-like arrangement of the bright atomic columns is very similar to that seen in the ordered η phase in the alloy Allvac 718Plus that has the same -ABACA- stacking as the five layers at the centre of the SESF [33]. This clear structure provides further evidence that the diffusive reordering scheme put forward by Kovarik *et al.* [14,16] is necessary for the propagation of the fault. In the SISFs the segregation is rather different. In the HAADF images, the brighter contrast appears diffuse and distributed uniformly throughout the fault and the adjacent planes. There is no discernible contrast between the atomic columns within the fault that would indicate a preference for specific sublattice sites on this much narrower fault.

The concept of reordering is a more precise description of the "atomic shuffles that were mentioned in the original work of Kear *et al.* [4–6] in which the $a\langle 112\rangle$ stacking fault ribbon structure was first introduced. Note that the extended nature of the ribbons in these samples precluded examination of each transition. However, the present HAADF observations provide direct insight into the structure of the leading and trailing superpartials, and the leading $\frac{a}{6}\langle 112\rangle$ dislocation of the SESF, as summarised in Figure 16. According to the structure of the dislocations bounding the SESF and SISF revealed in this work, three reordering reactions are required to propagate the $a\langle 112\rangle$ stacking fault ribbon. One at each end of the SESF, as has already been widely acknowledged [3–6], but additionally a reordering reaction at the leading edge of the SISF is required. The first occurs behind the leading $\frac{a}{3}\langle 112\rangle$ to produce an SISF from an APB and CSF. The second reordering step is necessary to lower the energy of the two-layer CISF (CESF-2) into an SESF. The final reordering step is required following the termination of the SESF to create a CISF in the trailing $\frac{a}{3}\langle 112\rangle$ superpartial core. This three-fold reordering process is very likely to be the rate determining step of the movement of this defect which plays such a major role in primary creep of the alloy CMSX-4.

For the first time it is confirmed that a reordering reaction is also required for the formation of the SISF which might be formed independent of a SESF by the dissociation of an $a\langle 110\rangle$ dislocation. In this case a second reordering would be needed to terminate the fault.

If the high atomic number elements segregate to the fault, this must result in a lower SISF energy. This reduction of energy would stabilise the SISF, and there would be a smaller driving force for SISF removal from the precipitates, resulting in a reduced rate of primary creep. Clearly, insight into both the structure of the dislocations and the segregation to the faults is extremely important in order to adequately account for the overall and relative mobility of each partial of the ribbon configuration.

Another important phenomenon observed in this study is the distortion of the γ/γ' interface by the dislocations, which results in it having a serrated appearance. This would undoubtedly have a marked effect on the climb of dislocations around the precipitates. While some limited growth of the γ' may have occurred during cooling from the test temperature, the observed distortion still reflects the effect of the stress on the energy balance between the interface position. If the atoms are mobile enough to produce the interface distortion upon cooling, they are clearly mobile enough do this during creep. The question then arises, whether a climbing dislocation would carry with it this interface profile or if this only happens to stationary dislocations. As all the γ lattice dislocations observed in the interface did have such a serration and were clearly climbing (as they were not aligned across the γ channels), this seems generally to be the case. The dislocation would need to constrict and shift the localised interface distortion with it as it moved. Interestingly some of the stacking faults crossing the γ/γ' interface also showed serrations whereas others did not; compare for example Figures 8 and 9. This lends weight to the argument that stacking faults can form by the combination of dislocations at the interface leaving a serration which would gradually anneal out.

5 Conclusions

HR STEM of single crystal superalloys allows a new level of detail to be achieved when studying creep processes. Owing to the ability to resolve individual atomic columns, information is revealed that would otherwise be difficult or impossible to obtain using conventional TEM and other microstructural characterisation techniques. Thus, HR STEM will undoubtedly prove an essential technique for furthering the scientific understanding of plasticity in superalloys. The main observations of this study can be summarised as follows:

(1) The $\frac{a}{3}\langle 112\rangle$ superpartials at the terminations of SISFs and SESFs in the

γ' dissociate into Shockley partial pairs bounding complex faults. superlattice dislocations that formed SISFs were terminated by two closely spaced Shockley partials of edge character and net Burgers vector $\frac{a}{6}[1\bar{1}2]$ separated by a CESF-1. This is consistent with the predictions made using PFMD with a two-layer γ-surface and atomistic calculations.

(2) The superlattice dislocations that formed an SESF in the γ' phase were consistent with the leading dislocations with a Burgers vector of either $\frac{a}{6}[211]$ or $\frac{a}{6}[\bar{1}\bar{2}1]$. These were not the trailing $\frac{a}{3}[1\bar{1}2]$ dislocations one would expect in primary creep. The SESF faults terminate with constricted intrinsic faults that are likely to have the CISF structure in the γ' phase and zonal dislocations at the γ/γ' interface.

(3) Extensive segregation of the heavier alloying element atoms to the stacking faults has been observed. In the case of the SISF, the segregation is diffuse and does not show any order. In the case of the SESF the segregation of heavy alloying elements appears to be ordered, forming a grid-like pattern in the fault. This strongly indicates that the SESF is formed by a vacancy mediated shuffle mechanism.

(4) Both the reordering process and segregation to the faults are critical considerations in determining the rate of movement of the stacking fault ribbons, and thus the creep rate.

(5) The γ/γ' interface is locally distorted by the stress fields around the dislocations. This is different from the planar interface structure that is often assumed for single crystal superalloys with high volume fractions of γ'.

6 Acknowledgements

The authors would like to acknowledge funding from the EPSRC under grant number EP/ D047684/1 (Alloys by Design) and thank Rolls-Royce plc. for supplying the CMSX-4 single crystals for this study.

References

[1] R. Decker, Strengthening mechanisms in nickel-base superalloys, in: Steel Strengthening Mechanisms (Symposium), Climax Molybdenum Company, Republished by TMS for Superalloys 2008, 1969, pp. 147–170.

[2] R. C. Reed, N. Matan, D. C. Cox, M. A. Rist, C. M. F. Rae, Acta Materialia 47 (12) (1999) 3367–3381.

[3] C. Rae, R. Reed, Acta Materialia 55 (3) (2007) 1067–1081.

[4] B. H. Kear, A. F. Giamei, G. R. Leverant, J. M. Oblak, Scripta Metallurgica 3 (2) (1969) 123–129.

[5] B. H. Kear, A. F. Giamei, G. R. Leverant, J. M. Oblak, Scripta Metallurgica 3 (7) (1969) 455–460.

[6] G. R. Leverant, B. H. Kear, Metallurgical Transactions 1 (1970) 491–498.

[7] M. Yamaguchi, D. Pope, V. Paidar, V. Vitek, Philosophical Magazine A 45 (5) (1982) 867–882.

[8] V. A. Vorontsov, C. Shen, Y. Wang, D. Dye, C. M. F. Rae, Acta Materialia 58 (12) (2010) 4110–4119.

[9] V. A. Vorontsov, R. Voskoboinikov, C. M. F. Rae, Advanced Materials Research 278 (2011) 150–155.

[10] V. A. Vorontsov, R. E. Voskoboinikov, C. M. F. Rae, Philosophical Magazine XXX (2011) XXXXX.

[11] R. Voskoboinikov, C. Rae, A new γ-surface in $\{111\}$ plane in $L1_2$ Ni_3Al, IOP Conference Series: Materials Science and Engineering 3 (1) (2009) 012009.

[12] T. Link, M. Feller-Kniepmeier, Metallurgical Transactions A 23 (1992) 99–105.

[13] T. Link, Scripta Metallurgica et Materialia 31 (6) (1994) 671–676.

[14] L. Kovarik, R. Unocic, J. Li, P. Sarosi, C. Shen, Y. Wang, M. Mills, Progress in Materials Science 54 (6) (2009) 839–873.

[15] R. Unocic, L. Kovarik, C. Shen, P. Sarosi, Y. Wang, J. Li, S. Ghosh, M. Mills, Deformation mechanisms in Ni-base disk superalloys at higher teemperatures, in: Superalloys 2008, TMS, 2008, pp. 377–385.

[16] L. Kovarik, R. Unocic, J. Li, M. Mills, JOM 61 (2) (2009) 42–48.

[17] D. Williams, C. Carter, Transmission Electron Microscopy, Second Edition, Springer, 2009.

[18] J. Li, Central symmetry parameter, http://mt.seas.upenn.edu/Archive/Graphics/A/Doc/CentralSymmetry.pdf, part of AtomEye online manual. (August 2003).

[19] A. Mottura, N. Warnken, M. Miller, M. Finnis, R. Reed, Acta Materialia 58 (3) (2010) 931–942.

[20] U. Hemmersmeier, M. Feller-Kniepmeier, Materials Science and Engineering: A 248 (1-2) (1998) 87–97.

[21] T. Link, A. Epishin, M. Paulisch, T. May, Materials Science and Engineering: A 528 (19-20) (2011) 6225–6234.

[22] U. Brückner, A. Epishin, T. Link, K. Dressel, Materials Science and Engineering: A 247 (1-2) (1998) 23–31.

[23] D. Dye, J. Coakley, V. Vorontsov, H. Stone, R. Rogge, Scripta Materialia 61 (2) (2009) 109–112.

[24] J. Hirth, J. Lothe, Theory of Dislocations, John Wiley & Sons, 1982.

[25] D. Siebörger, H. Knake, U. Glatzel, Materials Science and Engineering A 298 (1-2) (2001) 26–33.

[26] X. Nie, R. Wang, Y. Ye, Y. Zhou, D. Wang, Solid State Communications 96 (10) (1995) 729–734.

[27] Y. Mishin, Acta Materialia 52 (6) (2004) 1451–1467.

[28] K. Hemker, M. Mills, Philosophical Magazine A 68 (2) (1993) 305–324.

[29] H. Karnthaler, E. Mühlbacher, C. Rentenberger, Acta Materialia 44 (2) (1996) 547–560.

[30] A. F. Giamei, J. M. Oblak, B. H. Kear, W. H. Rand, in: Proceedings of the 29^{th} Annual Meeting of the Electron Microscopy Society of America, Claitors Pub. Div., Baton Rouge, 1971, p. 112.

[31] V. Paidar, M. Yamaguchi, D. P. Pope, V. Vitek, Philosophical Magazine A 45 (1982) 883–894.

[32] R. Voskoboinikov, C. Rae, Unpublished work, EAM Simulations.

[33] E. J. Pickering, H. Mathur, A. Bhowmik, O. M. D. M. Messé, J. Barnard, M. Hardy, R. Krakow, K. Loehnert, C. M. F. Rae, submitted to Acta Materialia.

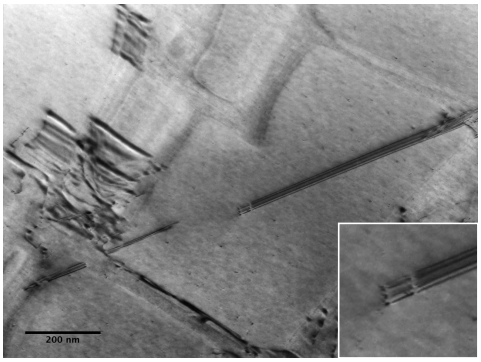

Fig. 1. TEM images showing stacking faults produced by an $\frac{a}{2}\langle 112\rangle$ dislocation during cutting of a γ' precipitate in a TMS-75 superalloy during primary creep at 750°C and 750MPa. A constricted stacking fault, which is likely to be complex, can be seen next to an extended one. Bright-field and dark-field images are shown on the left and right respectively.

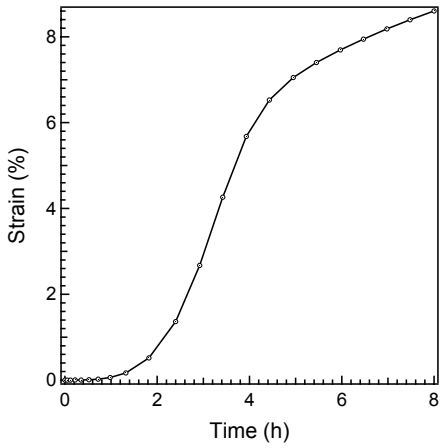

Fig. 2. Creep curve of the CMSX-4 single crystal test piece that was used to produce the HR STEM specimen foil. The test was carried out at 750°C and 750MPa. It can be seen that after experiencing an extended primary creep regime, the sample had undergone a significant amount of secondary creep as well.

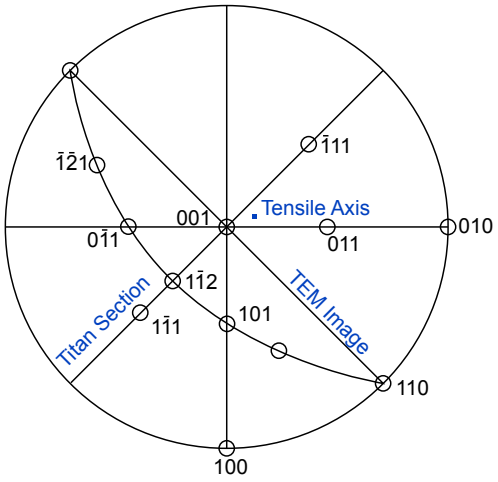

Fig. 3. Stereographic projection showing the orientation of the tensile axis, the TEM and HR STEM Image planes, as well as the observed active primary slip plane and Burgers vectors.

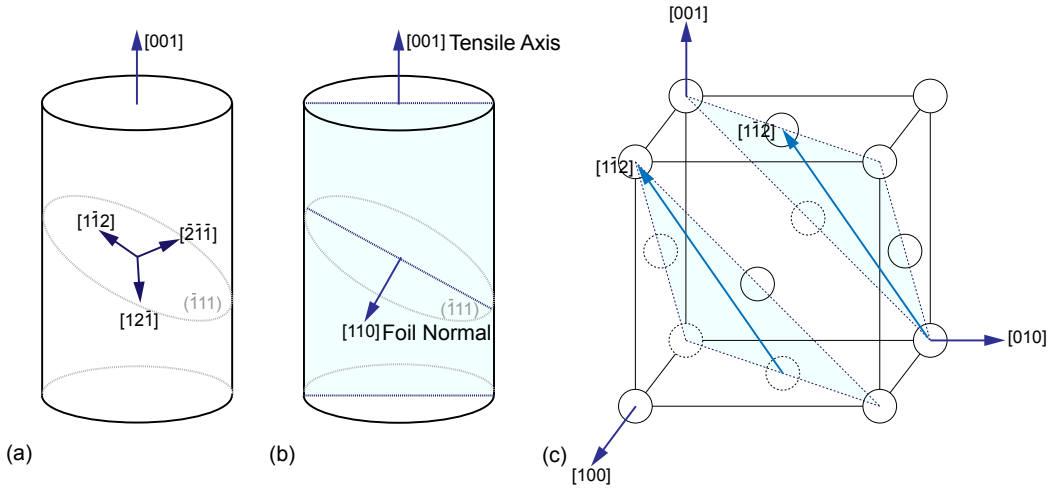

Fig. 4. Schematics showing the orientation of (a) the observed primary slip plane and the Burgers vectors with highest Schmid factor in the test specimen, (b) the HR STEM image plane relative to the test specimen and (c) the highest Schmid factor slip system within the unit cell.

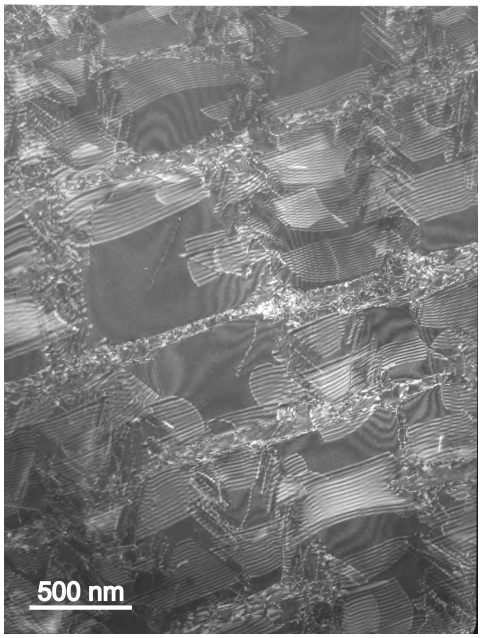

Fig. 5. Weak-beam bright-field TEM mage of the crept CMSX-4 single crystal specimen that was used for the HR STEM study. This TEM section was cut from the test piece perpendicularly to the HR STEM image plane, as is show in Figure 3. The primary slip plane lay at approximately 37° to the foil normal. It can be seen that there are numerous stacking faults within the γ' precipitates. The γ channels are saturated with numerous dislocations, that are the 'raw material' for forming the $a\langle 112\rangle$ and $a\langle 110\rangle$ superdislocations which are able to shear the precipitates

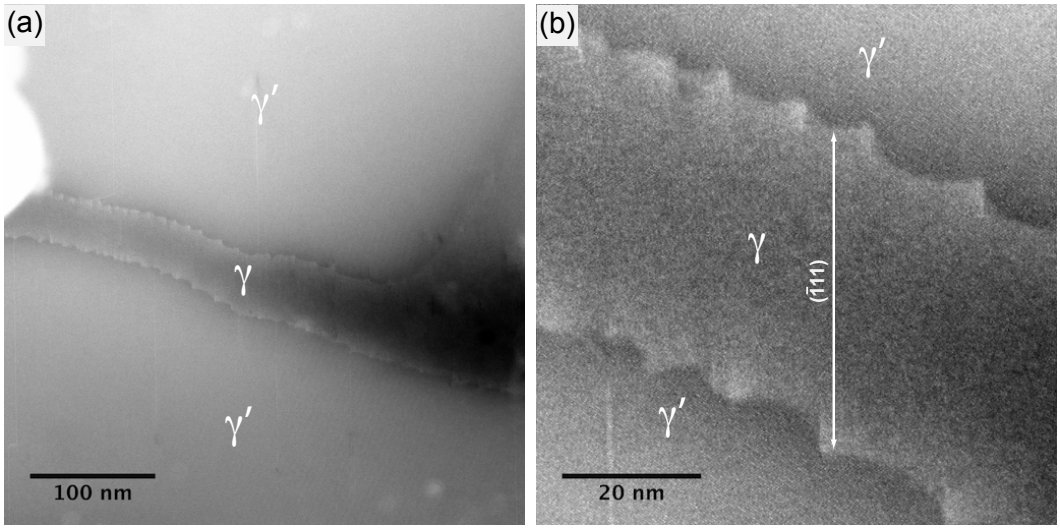

Fig. 6. HAADF images showing the serrated appearance of the γ/γ' interface in CMSX-4. This distortion is caused by the stress fields of the dislocations gliding through the material. Reference axes: vertical (bottom to top) - $[1\bar{1}2]$, horizontal (left to right) - $[1\bar{1}\bar{1}]$.

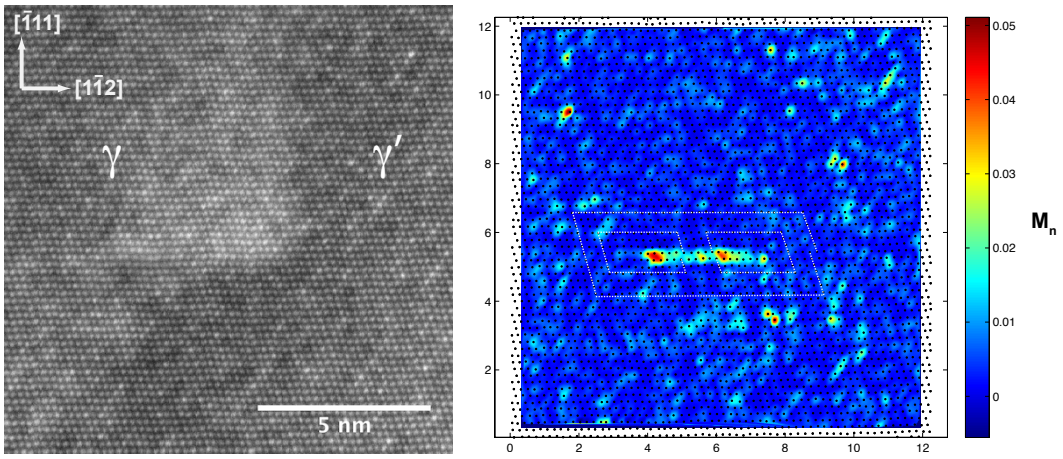

Fig. 7. An intrinsic stacking fault in the γ channel pinned at the matrix-precipitate interface. Raw HAADF image (a) and centro-symmetry analysis (b). Note that the spurious features in (b) are largely due to slight ripples in the STEM images which are artifacts created during the scanning process.

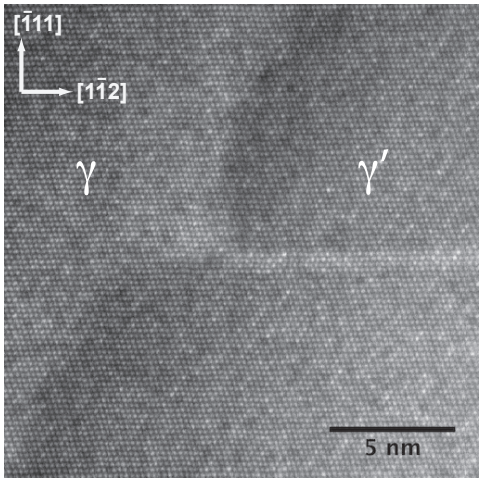

Fig. 8. HAADF image of an SISF within a γ' precipitate and terminating at the γ/γ' interface. The segregation of high Z elements at the fault makes it appear brighter than the surroundings.

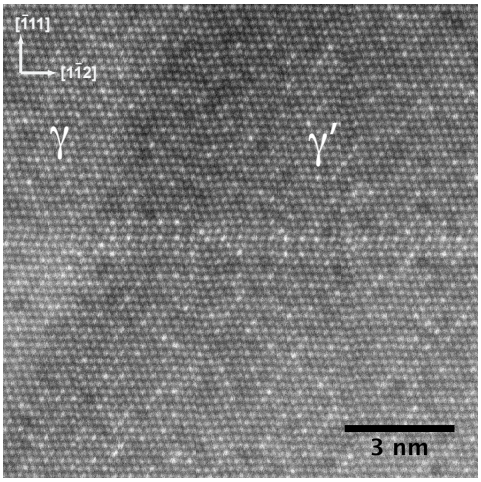

Fig. 9. HAADF image of an SESF terminating in the γ but close to the γ/γ' interface. Grid-like local ordering of high Z elements is visible within the fault.

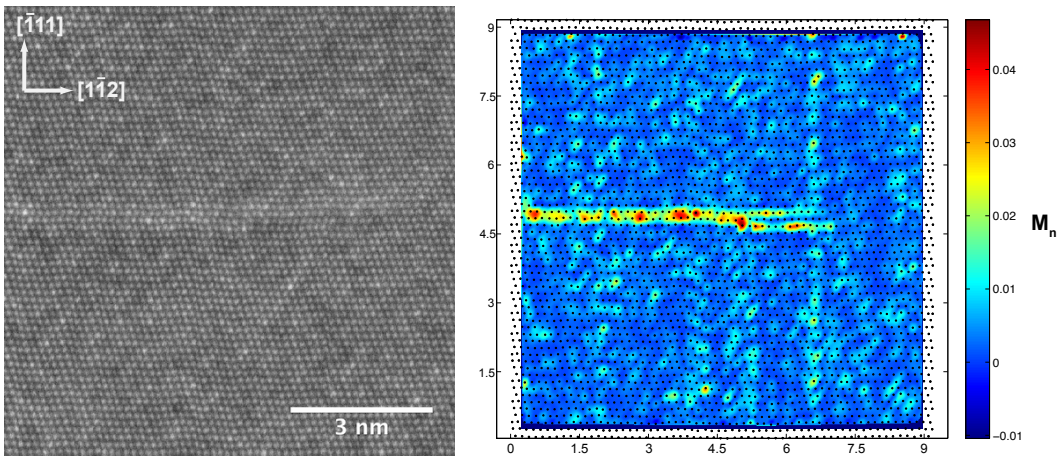

Fig. 10. An extended SISF terminating in a γ' precipitate. The terminating end shown here features a two layer CESF-1. Raw HAADF image (left) and centro-symmetry analysis (right).

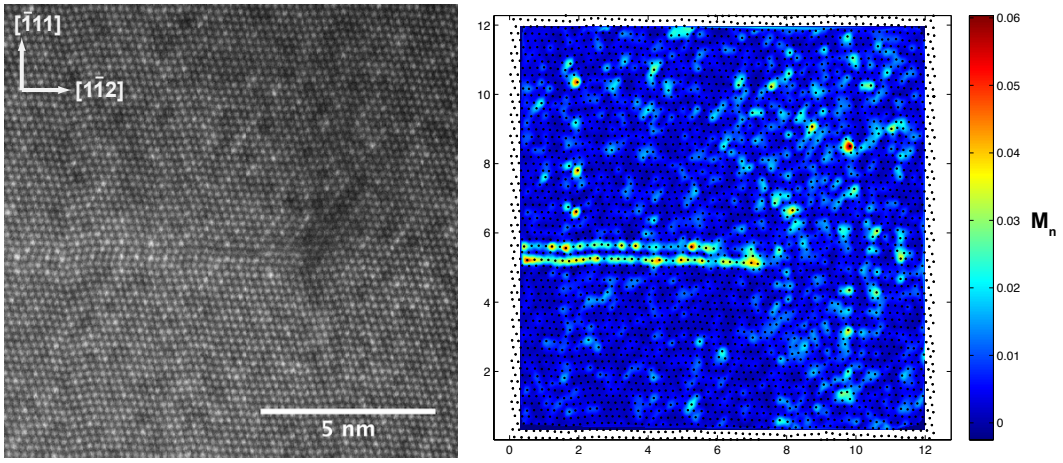

Fig. 11. An extended SESF terminating within a γ' precipitate. The terminating end shown here features CISF. Raw HAADF image (left) and centro-symmetry analysis (right).

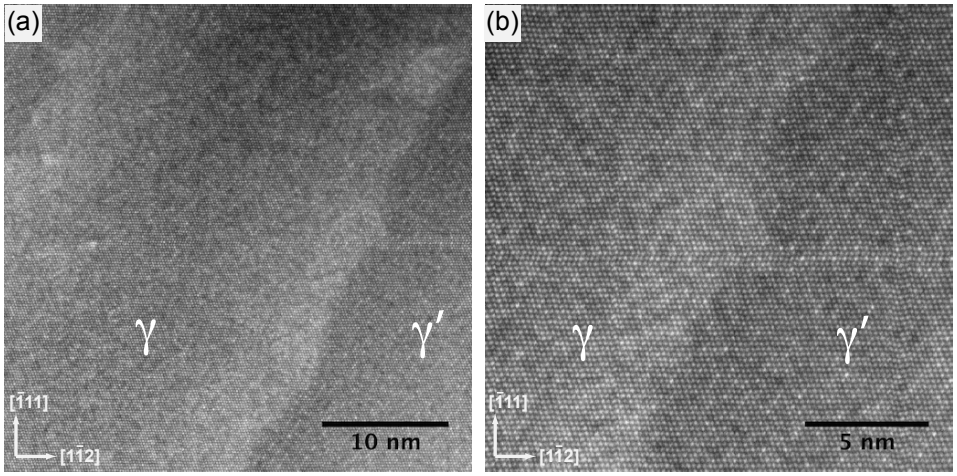

Fig. 12. HAADF image of an SESF crossing the γ/γ' interface.

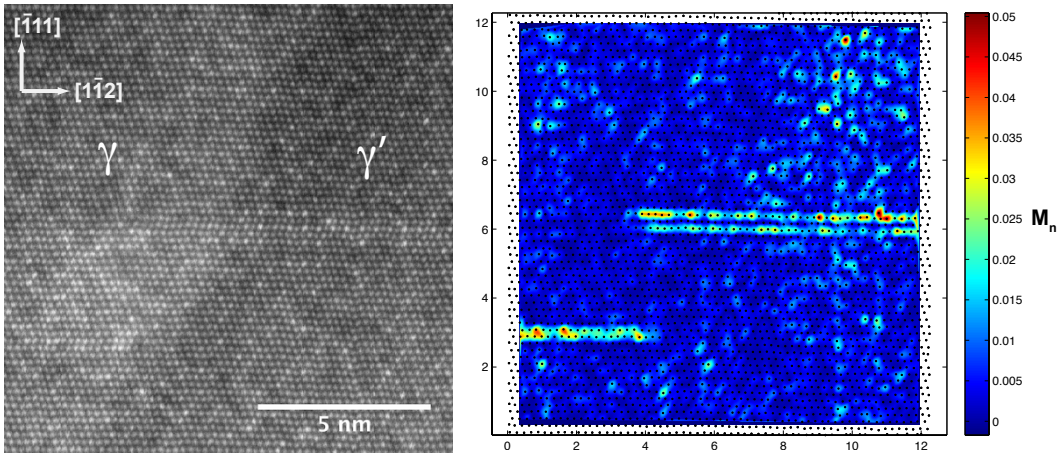

Fig. 13. Two stacking faults on parallel glide planes which have become pinned at the γ/γ' interface. On the left is an intrinsic fault in the γ, while on the right is an SESF in the γ'. (a) Raw HAADF image and (b) centro-symmetry analysis.

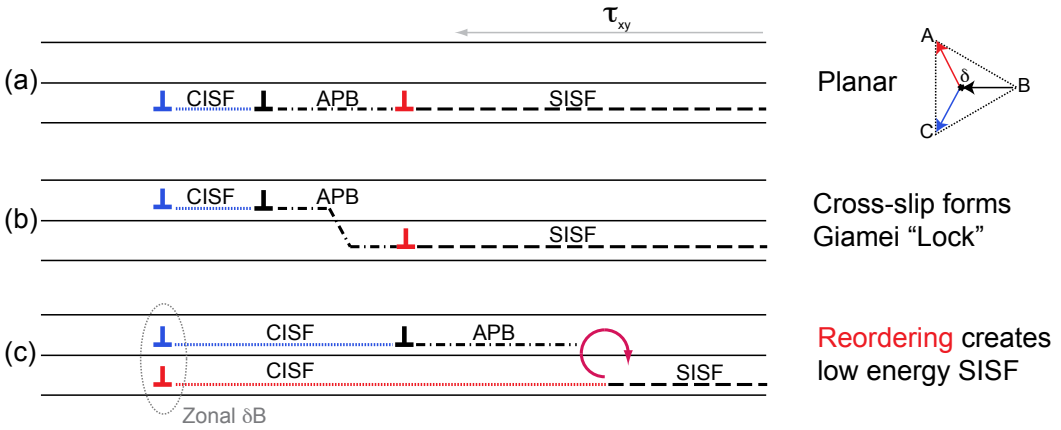

Fig. 14. Formation of SISF from planar configuration by cross-slip.

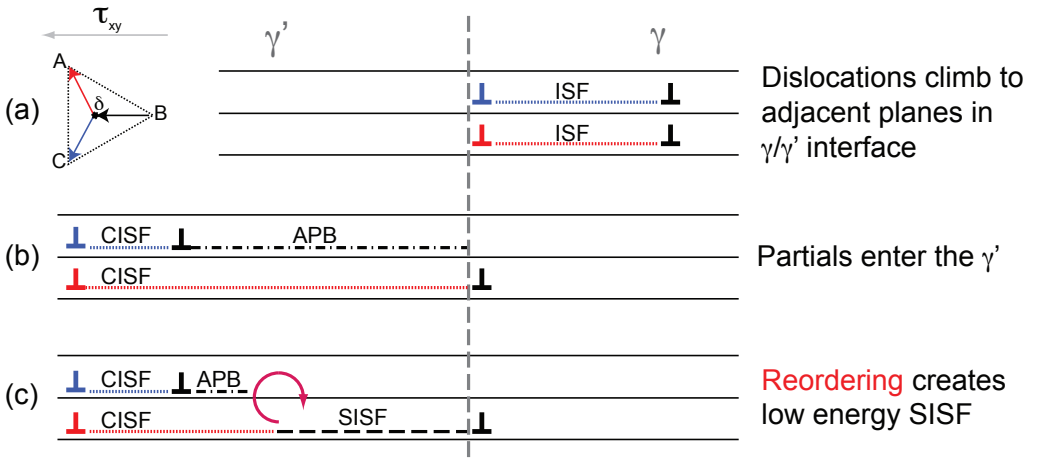

Fig. 15. Formation of SISF from two dislocations climbing in the γ/γ' interface.

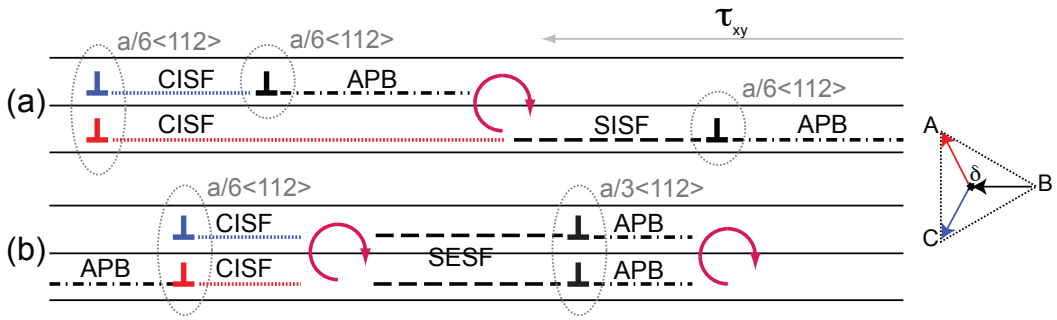

Fig. 16. Schematic of Stacking Fault ribbon $a\langle 112\rangle$ in γ' showing the leading (a) and trailing (b) $\frac{a}{2}\langle 112\rangle$ dislocations.